

ECLIPSING BINARIES IN THE OPEN CLUSTER RUPRECHT 147. III: THE TRIPLE SYSTEM EPIC 219552514 AT THE MAIN-SEQUENCE TURNOFF

GUILLELMO TORRES¹, ANDREW VANDERBURG^{2,3}, JASON L. CURTIS⁴, ADAM L. KRAUS², AARON C. RIZZUTO², AND MICHAEL J. IRELAND⁵

Accepted for publication in The Astrophysical Journal

ABSTRACT

Spectroscopic observations are reported for the 2.75 day, double-lined, detached eclipsing binary EPIC 219552514 located at the turnoff of the old nearby open cluster Ruprecht 147. A joint analysis of our radial velocity measurements and the *K2* light curve leads to masses of $M_1 = 1.509^{+0.063}_{-0.056} M_\odot$ and $M_2 = 0.649^{+0.015}_{-0.014} M_\odot$ for the primary and secondary, along with radii of $R_1 = 2.505^{+0.026}_{-0.031} R_\odot$ and $R_2 = 0.652^{+0.013}_{-0.012} R_\odot$, respectively. The effective temperatures are 6180 ± 100 K for the F7 primary and 4010 ± 170 K for the late K secondary. The orbit is circular, and the stars' rotation appears to be synchronized with the orbital motion. This is the third eclipsing system analyzed in the same cluster, following our earlier studies of EPIC 219394517 and EPIC 219568666. By comparison with stellar evolution models from the PARSEC series, we infer an age of $2.67^{+0.39}_{-0.55}$ Gyr that is consistent with the estimates for the other two systems. EPIC 219552514 is a hierarchical triple system, with the period of the slightly eccentric outer orbit being 463 days. The unseen tertiary is either a low-mass M dwarf or a white dwarf.

1. INTRODUCTION

Eclipsing binaries that are members of star clusters are particularly valuable objects for Astrophysics. When they happen to be double-lined, classical spectroscopic and lightcurve analysis techniques can yield accurate, model-independent masses and radii with precisions reaching a few percent in favorable cases (see, e.g., Andersen 1991; Torres 2010). For detached binaries, such measurements provide stringent constraints on stellar evolution theory in a population whose age, metallicity, and distance can be determined independently based, e.g., on spectroscopic observations and studies of their color-magnitude diagrams.

In recent work, we reported results for the eclipsing binaries EPIC 219394517 (Torres et al. 2018, hereafter Paper I) and EPIC 219568666 (Torres et al. 2019, Paper II) in the nearby old open cluster Ruprecht 147 (NGC 6774). Its members are slightly metal-rich compared to the Sun ($[\text{Fe}/\text{H}] = +0.10$; Curtis et al. 2018), and are located some 300 pc away. Both binaries gave consistent ages near 2.7 Gyr from a comparison with models of stellar evolution. While EPIC 219394517 (orbital period $P = 6.53$ days) is composed of very similar early G-type stars, the components of EPIC 219568666 ($P = 11.99$ days) are considerably different in mass (F8 and K5), and therefore provide greater leverage for testing theory.

In this paper, we present an analysis of a third, short period (2.75 days) but well detached eclipsing binary sys-

tem in the same cluster, EPIC 219552514. This object was observed by NASA's *K2* mission, the successor to the *Kepler* mission, during Campaign 7 (late 2015). Aliases include TYC 6296-1893-1, 2MASS J19162232-1627505, and Gaia DR2 4087856280717586560. A brief description of the object was presented by Curtis (2016). Its membership in Ruprecht 147 is supported by its position, proper motion, and parallax from the *Gaia*/DR2 catalog (Gaia Collaboration et al. 2018), as reported by Olivares et al. (2019), and also by its systemic radial velocity located at the peak of the distribution of measures for other cluster members (see Curtis et al. 2013; Yeh et al. 2019). EPIC 219552514 is quite bright ($Kp = 10.12$, $V = 10.34$), and has two distinguishing characteristics: it is found here to be a triple system for which we are able to determine the outer orbit, and it is located at the main-sequence turnoff of the cluster, making its properties (especially the radii) much more sensitive diagnostics of its evolutionary state. Because of this, it provides a valuable opportunity to further refine the age determination for Ruprecht 147, which can serve as a check on independent dating techniques such as asteroseismology and gyrochronology, when those become available for the cluster.

We begin our paper by presenting the photometric, imaging, and spectroscopic observations in Section 2, along with the procedures to detrend the photometry and to derive radial velocities. The joint analysis of the radial velocity measurements and *K2* light curve is described in Section 3. The results are then used to infer the absolute properties of EPIC 219552514 in Section 4. Rotation and activity are discussed in Section 4.1, and Section 5 deals with a comparison of the masses, radii, and temperatures against current models of stellar evolution in order to infer the age. Concluding remarks are found in Section 6.

2. OBSERVATIONS

¹ Center for Astrophysics | Harvard & Smithsonian, 60 Garden St., Cambridge, MA 02138, USA; gtorres@cfa.harvard.edu

² Department of Astronomy, The University of Texas at Austin, Austin, TX 78712, USA

³ NASA Sagan Fellow

⁴ American Museum of Natural History, Central Park West, New York, NY, USA

⁵ Research School of Astronomy and Astrophysics, Australian National University, Canberra, ACT 2611, Australia

Table 1
Detrended *K2* Photometry of
EPIC 219552514

HJD (2,400,000+)	Residual flux
57301.4866	0.99947727
57301.5070	0.99939460
57301.5275	0.99938356
57301.5479	0.99946419
57301.5683	0.99970927

Note. — *K2* photometry after removal of instrumental effects and long-term drifts. (This table is available in its entirety in machine-readable form.)

2.1. Photometry

EPIC 219552514 was observed by the *K2* mission during its Campaign 7, as part of a large super-aperture targeting the core of Ruprecht 147. The observations were made in long cadence mode, once every 29.4 minutes. We downloaded the superstamp observations from the Mikulski Archive for Space Telescopes (MAST)⁶, extracted light curves for cluster members following Vanderburg & Johnson (2014) and Vanderburg et al. (2016), and initially identified EPIC 219552514 as an eclipsing binary. A total of 30 primary eclipses and 29 secondary eclipses are included in the 81 days of photometric coverage. Because the object is in a fairly crowded region of the sky, we re-extracted a raw light curve following the procedure from previous papers in our series (Torres et al. 2018, 2019) using a circular moving aperture with a radius of $15''.8$, in order to ensure that the third-light contamination in the lightcurve is constant (and not dependent on the roll of the *K2* spacecraft). We used a first pass systematics correction as in Vanderburg & Johnson (2014) and Vanderburg et al. (2016), and then took this as a starting point for a simultaneous fit of the *K2* 6-hour roll systematics, the primary and secondary eclipses, and out-of-eclipse variability. Further details may be found in our previous studies. We subsequently removed long term trends with a low-order spline. The photometry processed in this way is provided in Table 1, and is used below for our lightcurve analysis.

2.2. Spectroscopy

EPIC 219552514 was monitored spectroscopically at the Center for Astrophysics for three years beginning in 2016 September, with the fiber-fed, bench-mounted Tillinghast Reflector Echelle Spectrograph (TRES; Szentgyorgyi & Fűrész 2007; Fűrész 2008) attached to the 1.5m Tillinghast reflector at the Fred L. Whipple Observatory on Mount Hopkins (Arizona, USA). We collected a total of 43 spectra, at a resolving power of $R \approx 44,000$ and covering the wavelength region 3800–9100 Å in 51 orders. For the order centered at ~ 5187 Å containing the Mg I b triplet, the signal-to-noise ratios range from 46 to 100 per resolution element of 6.8 km s^{-1} .

While visual examination shows the spectra to be only single-lined, the radial velocity of the very weak secondary lines can be measured in most cases using TODCOR, a two-dimensional cross-correlation technique introduced by Zucker & Mazeh (1994). Templates matching the properties of each component were taken from a pre-computed library of synthetic spectra that are based on model atmospheres by R. L. Kurucz, and a line list tuned to better match the spectra of real stars (see Nordström et al. 1994; Latham et al. 2002). These templates cover a limited wavelength region of ~ 300 Å centered around 5187 Å.

The effective temperature (T_{eff}) and projected rotational velocity ($v \sin i$) of the primary star were determined following the procedure described by Torres et al. (2002), by running grids of one-dimensional cross-correlations of the observed spectra against synthetic spectra over broad ranges in those two parameters. We ignored the presence of the faint secondary, as it does not affect the results. We then selected the combination of parameters giving the highest value of the cross-correlation coefficient averaged over all 43 spectra, weighted by the strength of each exposure. We repeated this for fixed values of the surface gravity ($\log g$) of 3.5 and 4.0, bracketing the final values reported below in Section 4, and for metallicities $[\text{Fe}/\text{H}]$ of 0.0 and +0.5 on either side of the known cluster abundance. By interpolation we obtained $T_{\text{eff}} = 6180 \text{ K}$ and $v \sin i = 49 \text{ km s}^{-1}$, with estimated uncertainties of 100 K and 3 km s^{-1} , respectively. These errors are based on the scatter from the individual spectra, conservatively increased to account for possible systematic errors. The corresponding spectral type for the primary is approximately F7. For the radial velocity determinations of this star, we used template parameters of 6250 K and 50 km s^{-1} , which are the nearest in our grid, along with $\log g = 4.0$ and $[\text{Fe}/\text{H}] = 0.0$.

The lines of the secondary are too weak for us to determine its temperature or its rotational velocity directly from our spectra. For the purpose of measuring radial velocities, we therefore used a template with $T_{\text{eff}} = 4000 \text{ K}$ appropriate for star of its mass as determined later (spectral type late K). In Section 4 below we provide an empirical estimate of the secondary temperature that supports this choice. For the rotation, we adopted $v \sin i = 12 \text{ km s}^{-1}$ assuming that its spin is synchronized with the orbital motion, and using a typical radius for a star of this type. The metallicity for the secondary template was kept at the solar value as for the primary, and $\log g$ was set to 4.5.

Each of the 43 spectra yielded a precise radial velocity measurement for the primary, but the secondary lines were clearly visible in only 31 of them. The heliocentric velocities for both stars in EPIC 219552514 are presented in Table 2, along with their formal uncertainties. The secondary velocities are much poorer because of its faintness. Using TODCOR we estimated the average secondary-to-primary flux ratio at the mean wavelength of our observations (5187 Å) to be only $\ell_2/\ell_1 = 0.0035 \pm 0.0010$, the smallest we have ever measured with this instrument for any star.

A preliminary orbital solution based on these velocities showed an obvious long-term periodic pattern in the

⁶ <http://archive.stsci.edu/>

Table 2
Heliocentric Radial-velocity Measurements of EPIC 219552514

HJD (2,400,000+)	RV ₁ (km s ⁻¹)	RV ₂ (km s ⁻¹)	Inner Phase	Outer Phase
57647.6200	-20.98 ± 0.38	...	0.7552	0.0738
57853.9799	-13.71 ± 0.33	182.93 ± 11.51	0.6978	0.5191
57857.9907	90.89 ± 0.27	-62.88 ± 9.39	0.1544	0.5277
57863.9704	94.87 ± 0.31	-86.73 ± 10.89	0.3260	0.5406
57878.9624	-15.33 ± 0.22	169.53 ± 7.67	0.7706	0.5730
57879.9634	87.33 ± 0.21	-56.32 ± 7.46	0.1341	0.5751
57885.9000	100.55 ± 0.23	...	0.2901	0.5879
57900.9030	-14.16 ± 0.23	...	0.7386	0.6203
57906.8573	10.28 ± 0.20	...	0.9010	0.6331
57907.9249	101.66 ± 0.20	-92.58 ± 7.01	0.2887	0.6354
57908.8536	2.35 ± 0.23	128.76 ± 8.08	0.6260	0.6374
57910.8995	88.14 ± 0.33	-69.46 ± 11.54	0.3690	0.6419
57914.9432	-4.84 ± 0.26	165.37 ± 9.22	0.8375	0.6506
57919.8292	6.84 ± 0.22	144.13 ± 7.79	0.6120	0.6611
57932.9240	88.91 ± 0.25	-45.51 ± 8.60	0.3675	0.6894
57965.7724	102.98 ± 0.26	-98.09 ± 9.04	0.2969	0.7603
58001.6828	96.93 ± 0.26	...	0.3383	0.8377
58002.6854	-10.32 ± 0.24	170.88 ± 8.58	0.7024	0.8399
58020.6379	104.28 ± 0.23	...	0.2221	0.8786
58034.6044	101.65 ± 0.20	...	0.2943	0.9088
58035.5836	-2.20 ± 0.23	151.53 ± 8.08	0.6499	0.9109
58037.5873	86.33 ± 0.24	-45.23 ± 8.51	0.3775	0.9152
58050.5881	78.15 ± 0.25	-38.64 ± 8.68	0.0990	0.9433
58056.5695	102.00 ± 0.24	-93.30 ± 8.34	0.2712	0.9562
58060.5644	-15.34 ± 0.22	181.35 ± 7.83	0.7220	0.9648
58068.5504	0.61 ± 0.28	134.30 ± 9.66	0.6222	0.9820
58259.9510	82.52 ± 0.22	-51.94 ± 7.60	0.1321	0.3950
58276.8394	99.05 ± 0.38	...	0.2654	0.4314
58277.9011	-8.36 ± 0.24	147.55 ± 8.36	0.6510	0.4337
58279.8654	84.53 ± 0.21	...	0.3644	0.4380
58290.8725	85.49 ± 0.19	-52.88 ± 6.69	0.3618	0.4617
58301.8394	89.74 ± 0.21	-85.32 ± 7.44	0.3445	0.4854
58331.9025	101.77 ± 0.42	-95.65 ± 14.71	0.2624	0.5502
58386.7016	95.58 ± 0.27	-66.91 ± 9.32	0.1635	0.6685
58594.9671	-19.88 ± 0.31	...	0.7981	0.1178
58601.9686	86.14 ± 0.25	-71.51 ± 8.85	0.3408	0.1329
58621.9451	2.58 ± 0.27	122.40 ± 9.59	0.5956	0.1760
58628.8947	75.78 ± 0.21	-49.69 ± 7.28	0.1194	0.1910
58634.9162	91.20 ± 0.23	-88.82 ± 8.10	0.3062	0.2040
58660.8715	-21.93 ± 0.27	172.06 ± 9.36	0.7323	0.2600
58674.8176	-19.51 ± 0.30	169.69 ± 10.50	0.7970	0.2901
58693.7778	-15.90 ± 0.30	...	0.6827	0.3310
58744.6811	91.77 ± 0.34	...	0.1690	0.4408

Note. — Orbital phases for the inner orbit are counted from the reference time of primary eclipse, and those for the outer orbit from the corresponding time of periastron passage. The final velocity uncertainties for our analysis result from scaling the values listed here for the primary and secondary by the near-unity factors f_1 and f_2 , respectively, from our global analysis described in Section 3.

residuals of the primary star, with a peak-to-peak amplitude of about 10 km s⁻¹. This indicates the presence of a third component in the system. However, careful examination of our spectra with TRICOR, an extension of TODCOR to three dimensions (Zucker et al. 1995), showed no sign of a third set of lines. This suggests that the tertiary must be even fainter than the secondary, possibly a mid or late M dwarf.

A preliminary fit to the velocities was performed to serve as a starting point for the analysis of Section 3, solving for the elements of the inner and outer orbits simultaneously assuming they are represented by independent Keplerian trajectories. The outer orbit is slightly eccentric ($e \approx 0.19$) and has a period of about 463 days that is covered more than twice by our observations. The inner orbit for the eclipsing pair, on the other hand, shows no significant eccentricity.

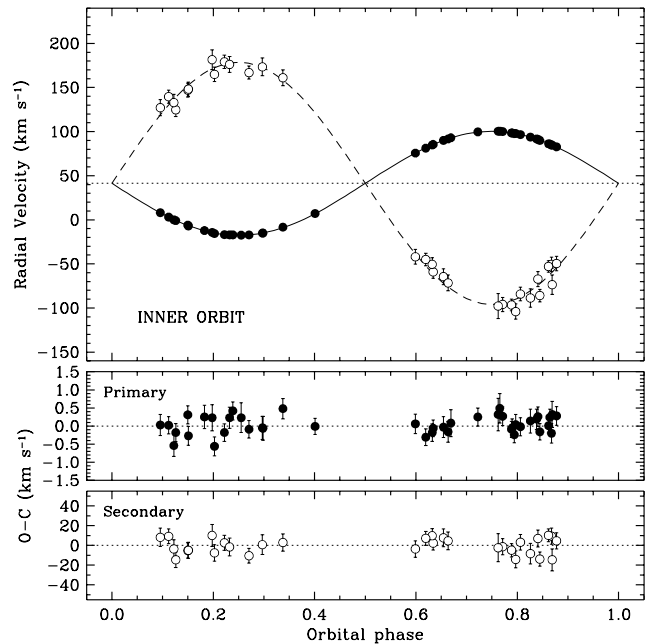


Figure 1. Radial-velocity measurements for EPIC 219552514, with our adopted model for the inner orbit from Section 3. Primary and secondary measurements are represented with filled and open circles, respectively, and have the motion in the outer orbit removed. The dotted line marks the center-of-mass velocity of the triple system. Error bars for the primary are too small to be visible. They are seen in the lower panels, which display the residuals. Phases are counted from the reference time of primary eclipse (Table 4).

Figure 1 displays the velocities of the primary and secondary in the inner (2.75 day) orbit after subtracting the motion in the outer orbit, as described below. Our final model is also shown. The motion of the primary star in the outer orbit is illustrated in Figure 2, in which we have removed the short-period motion in the inner orbit.

2.3. Imaging

The aperture we used to extract the photometry of EPIC 219552514 appears fairly clear of any intruding stars bright enough to add significant flux to the light curve and bias the results of our analysis below. This is shown in Figure 3, which is a seeing-limited image in a bandpass similar to Sloan r (close to *Kepler*'s Kp bandpass) taken in 2008 by Curtis et al. (2013) with the MegaCam instrument (Hora et al. 1994) on the Canada-France-Hawaii Telescope (CFHT). The positions of all numbered stars in or near the aperture, their separations ρ from the target, and their brightness in the CFHT gri filters⁷, are given in Table 3 when bright enough to measure. We include also J - and K -band brightness measurements based on UKIRT/WFCAM imaging (Curtis 2016), which reaches deeper. We additionally report the G -band magnitude and trigonometric parallax, when available, for the few companions that have entries in the *Gaia*/DR2 catalog (Gaia Collaboration et al. 2018). None appear to be members of the cluster. All companions within the aperture are very faint and have no effect on our analysis. Even the two brighter ones that are slightly outside the aperture (#21 and #24) will not

⁷ <http://www.cadc-ccda.hia-ihp.nrc-cnrc.gc.ca/en/megapipe/docs/filtold.html>

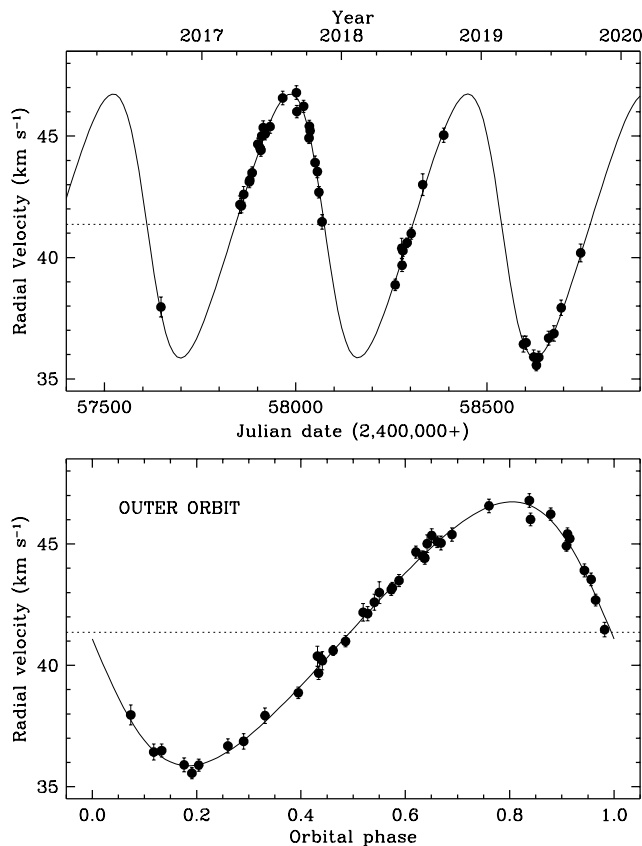


Figure 2. Radial-velocity measurements for the primary of EPIC 219552514 in the outer orbit, as a function of time (top) and orbital phase counted from periastron passage (bottom). Motion in the inner orbit has been removed. The secondary has much larger scatter and is not shown, for clarity. The solid line is our final model from Section 3, and the dotted line represents the center-of-mass velocity of the triple.

contribute significantly: they are more than 6 magnitudes fainter than the target in the near infrared, they are fairly red (SpT \sim K3 and K5, respectively) and will therefore appear even fainter in the Kp band, and only a small fraction of their flux would be inside the aperture given the *Kepler* pixel scale of $3''.98 \text{ pix}^{-1}$.

In order to search for blended stellar companions to EPIC 219552514 inside the inner working angle of the seeing-limited imaging, we used the 10m Keck II telescope with the NIRC2 facility adaptive optics (AO) imager to obtain natural guide star adaptive optics imaging and non-redundant aperture mask interferometry (NRM). These observations were made in the K' filter ($\lambda = 2.124 \mu\text{m}$) on 2016 June 16 UT, and followed the standard observing strategy described by Kraus et al. (2016) and previously reported for Ruprecht 147 targets by Torres et al. (2018) and Torres et al. (2019). For EPIC 219552514, we obtained a short sequence of 6 images and 8 interferograms in vertical angle mode. In both cases, calibrators were drawn from the other Ruprecht 147 members observed on the same night.

The images were analyzed following the methods described by Kraus et al. (2016). To summarize, the primary star point spread function (PSF) was subtracted using both an azimuthal median profile and the calibrator that most closely matches the speckle pattern. Within each image, the residual fluxes as a function of

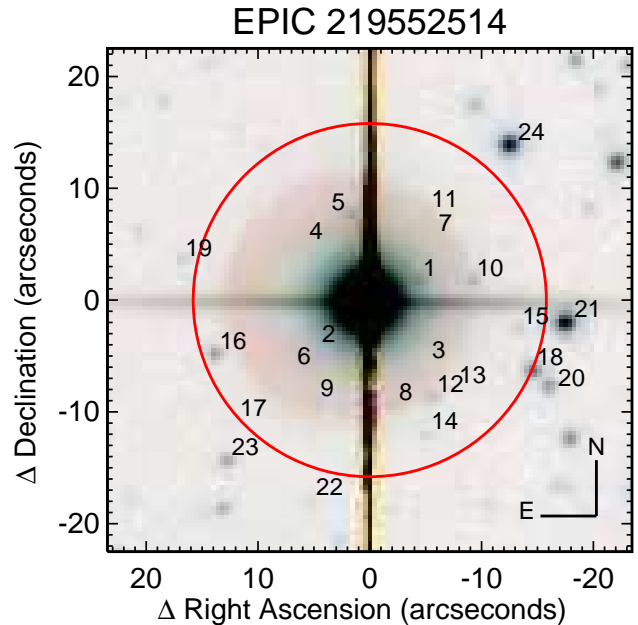


Figure 3. CFHT r -band image of the field of EPIC 219552514, with the $15''/8$ photometric aperture used to extract the $K2$ photometry indicated with a circle. Nearby companions are numbered as in Table 3.

position were measured in apertures of radius 40 milli-arcseconds (mas), centered on each pixel, and the noise was estimated from the RMS of fluxes within concentric rings around the primary star. Finally, the detections and detection limits were estimated from the flux-weighted sum of the detection significances in the stack of all images, and any location with a total significance greater than 6σ was visually inspected to determine if it was a residual speckle or cosmic ray. No candidates remained after this visual inspection. The observations yielded contrast limits of $\Delta K' = 5.6 \text{ mag}$ at $\rho = 150 \text{ mas}$, $\Delta K' = 7.7 \text{ mag}$ at $\rho = 500 \text{ mas}$, and $\Delta K' = 9.0 \text{ mag}$ at $\rho > 1000 \text{ mas}$.

The interferograms were analyzed following the methods described by Kraus et al. (2008) and Ireland (2013). We Fourier-transformed the interferograms to extract the complex visibilities, and from those we computed the corresponding closure phases for each triplet of baselines. We calibrated the closure phases with other observations of targets nearby on the sky and in time, and then fit the calibrated closure phases with binary source models to search for significant evidence of a companion, but did not find any. We determined the detection limits using a Monte Carlo process that randomizes the phase errors and determines the distribution of possible binary fits, indicating the 99.9% upper limit on companions in bins of projected separation. The observations yielded contrast limits of $\Delta K' = 0.13 \text{ mag}$ at $\rho = 20\text{--}40 \text{ mas}$, $\Delta K' = 1.22 \text{ mag}$ at $\rho = 40\text{--}80 \text{ mas}$, and $\Delta K' = 0.73 \text{ mag}$ at $\rho = 80\text{--}160 \text{ mas}$.

3. ANALYSIS

For the analysis of the $K2$ light curve, we adopted the Nelson-Davis-Etzel binary model (Etzel 1981; Popper & Etzel 1981) as implemented in the `eb` code of Irwin et al. (2011). This model approximates the star shapes as biaxial spheroids for calculating proximity effects, and is adequate for well-detached systems in which the stars are nearly spherical, as is the case here (see

Table 3
Close Neighbors of EPIC 219552514

#	R.A. (J2000)	Dec. (J2000)	P.A. (degree)	ρ ($''$)	J (mag)	K (mag)	σ_{JK} (mag)	g (mag)	r (mag)	i (mag)	σ_{gri} (mag)	G (mag)	π_{Gaia} (mas)
1	19:16:22.01	-16:27:48.9	295.2	5.2	17.05	16.28	0.02
2	19:16:22.61	-16:27:54.8	132.4	5.7	17.66	16.65	0.02
3	19:16:21.96	-16:27:56.2	226.1	7.6	18.67	17.54	0.05
4	19:16:22.69	-16:27:45.6	43.5	7.7	18.52	17.51	0.04
5	19:16:22.42	-16:27:43.0	9.3	8.2	18.07	17.44	0.04	20.72	...
6	19:16:22.76	-16:27:56.8	132.8	8.6	18.82	19.00	0.17
7	19:16:21.92	-16:27:44.9	316.4	8.8	18.94	18.35	0.09
8	19:16:22.16	-16:27:60.0	195.8	9.3	19.47	18.59	0.12
9	19:16:22.63	-16:27:59.6	153.6	9.6	19.30	18.02	0.08
10	19:16:21.69	-16:27:49.0	283.0	9.8	19.06	18.61	0.12	20.80	...
11	19:16:21.96	-16:27:42.7	327.6	10.0	19.43	19.02	0.17
12	19:16:21.93	-16:27:59.3	214.9	10.2	20.12	19.72	0.32
13	19:16:21.80	-16:27:58.5	226.0	10.9	20.44	18.88	0.23
14	19:16:21.96	-16:28:02.6	204.7	12.8	19.83	19.43	0.25
15	19:16:21.42	-16:27:53.2	260.8	13.8	19.57	19.19	0.20	23.29	22.41	21.99	0.07
16	19:16:23.22	-16:27:55.5	108.9	14.1	18.67	18.34	0.09	20.83	20.40	20.23	0.14	20.19	1.68 \pm 0.80
17	19:16:23.11	-16:28:01.4	132.8	15.5	19.60	17.97	0.11
18	19:16:21.34	-16:27:56.9	247.8	16.0	17.43	16.82	0.02	20.04	19.26	18.91	0.02	19.24	0.63 \pm 0.37
19	19:16:23.43	-16:27:47.2	76.1	16.9	19.55	18.69	0.13	23.53	22.55	22.30	0.07
20	19:16:21.24	-16:27:58.2	245.5	17.9	18.55	18.00	0.07	20.90	20.13	19.91	0.02	20.25	0.48 \pm 0.88
21	19:16:21.14	-16:27:52.6	264.9	17.9	15.86	15.30	0.01	17.44	-0.11 \pm 0.12
22	19:16:22.65	-16:28:08.5	165.3	18.1	19.63	19.28	0.21
23	19:16:23.15	-16:28:05.0	139.6	18.6	18.47	17.79	0.06	21.52	20.58	20.27	0.03	20.43	0.90 \pm 0.90
24	19:16:21.48	-16:27:36.7	319.5	19.2	15.82	15.14	0.01	18.54	17.63	17.28	0.01	17.65	0.27 \pm 0.15

Note. — Coordinates based on UKIRT images (see Curtis 2016). Average uncertainties σ_{JK} and σ_{gri} are listed for the corresponding magnitude measurements.

below). The main adjustable parameters we considered for the inner binary are as follows: the orbital period (P_{in}), a reference epoch of primary eclipse (T_0 , which is strictly the time of inferior conjunction in this code), the central surface brightness ratio in the *Kepler* bandpass ($J \equiv J_2/J_1$), the sum of the relative radii normalized by the semimajor axis ($r_1 + r_2$) and their ratio ($k \equiv r_2/r_1$), the cosine of the inclination angle ($\cos i$), the eccentricity parameters $e_{\text{in}} \cos \omega_{\text{in}}$ and $e_{\text{in}} \sin \omega_{\text{in}}$, with e_{in} being the eccentricity and ω_{in} the longitude of periastron for the primary, and an out-of-eclipse brightness level in magnitude units (m_0). We adopted a quadratic limb-darkening law for this work, with coefficients u_1 and u_2 for the primary and a corresponding set for the secondary. The reflection albedos (A_1, A_2) were included as additional variables. Gravity darkening coefficients for the *Kepler* band were adopted from the theoretical calculations by Claret & Bloemen (2011), interpolated to the metallicity of Ruprecht 147, the temperatures indicated earlier, and the final $\log g$ values reported below. They were held fixed at the values $y_1 = 0.306$ for the primary and $y_2 = 0.460$ for the secondary.⁸

Even though there is no evidence of significant flux from neighboring stars in the photometric aperture, as a precaution we included the third light parameter ℓ_3 as an additional adjustable parameter because the unseen tertiary (presumably a very red star) may be brighter in the *Kepler* band (centered around 6000 Å) than in our spectroscopic window (~ 5187 Å). Third light is defined here such that $\ell_1 + \ell_2 + \ell_3 = 1$, and the values for the primary and secondary for this normalization correspond to the light at first quadrature.

⁸ Note that these are bandpass-specific *coefficients*, not to be confused with the bolometric gravity darkening *exponents* used in other eclipsing binary modeling programs (see Torres et al. 2017).

To avoid biases, the finite integration time of the *K2* long-cadence observations was accounted for by oversampling the model light curve and then integrating over the 29.4-minute duration of each cadence prior to the comparison with the observations (see Gilliland et al. 2010; Kipping 2010).

The radial velocities were included in the analysis along with the photometry, and the spectroscopic elements for the inner and outer orbits were solved simultaneously as done in Section 2.2. This introduces the following additional elements: the primary and secondary velocity semiamplitudes (K_1 and K_2), the center-of-mass velocity of the triple system (γ), the outer orbital period (P_{out}), a reference time of periastron passage for the outer orbit (T_{peri}), the velocity semiamplitude of the inner binary in the outer orbit (K_{out}), and the eccentricity parameters $e_{\text{out}} \cos \omega_{\text{out}}$ and $e_{\text{out}} \sin \omega_{\text{out}}$, where ω_{out} corresponds to the longitude of periastron of the inner binary. We point out here that a mismatch between our cross-correlation templates and the real stars can potentially introduce a spurious systematic offset between the measured primary and secondary velocities. Because the template parameters adopted for the secondary, particularly $v \sin i$, are merely educated guesses, we allowed for such an offset (ΔRV) that we added to the list of free parameters.

Light travel time in the outer orbit will cause the eclipses to arrive slightly earlier or later than they would in the absence of the tertiary. Over the ~ 80 days of the *K2* observations the effect varies between -1.6 and -2.3 minutes (eclipses occur earlier), which is significant compared to the final precision we report for T_0 below. Consequently, we accounted for this effect during the analysis. This was done by appropriately adjusting all times of observation based on a estimate of those corrections from a preliminary model that used the radial velocities alone.

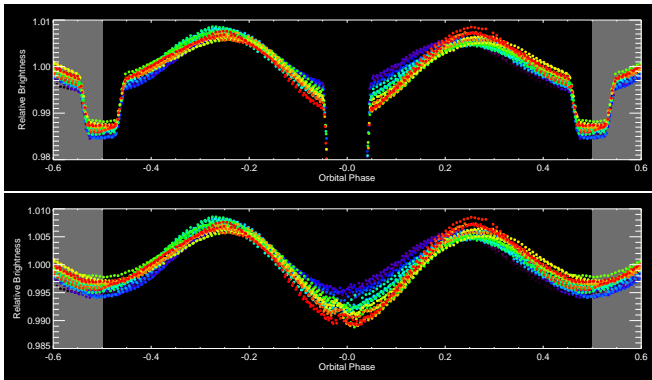


Figure 4. Phase-folded photometry of EPIC 219552514, color-coded by date to show the evolution of lightcurve distortions presumably caused by spots. Red points correspond to earlier data, and purple points to later data. The bottom panel has the eclipses removed, and reveals what appears to be a spot-crossing event (bump) during the primary eclipse in the early observations (red), which gradually disappears and is no longer seen in the later data (purple).

Our method of solution used the `emcee`⁹ code of Foreman-Mackey et al. (2013), which is a Python implementation of the affine-invariant Markov chain Monte Carlo (MCMC) ensemble sampler proposed by Goodman & Weare (2010). We used 100 walkers with chain lengths of 15,000 each, after discarding the burn-in. Uniform (non-informative) or log-uniform priors over suitable ranges were adopted for most adjustable parameters (see below), and convergence was verified by examining the chains visually and by requiring a Gelman-Rubin statistic of 1.05 or smaller for each parameter (Gelman & Rubin 1992). For more efficient sampling of parameter space, and to reduce the correlation between them, the traditional quadratic limb-darkening coefficients u_1 and u_2 for each star were recast as q_1 and q_2 following Kipping (2013), where $q_1 = (u_1 + u_2)^2$ and $q_2 = 0.5u_1/(u_1 + u_2)$.

The relative weighting between the photometry and radial velocity measurements was handled by introducing additional free parameters in the form of multiplicative scale factors for the observational errors. These scale factors (f_{K2} for the photometry, and f_1 and f_2 for the primary and secondary velocities) were solved for self-consistently and simultaneously with the other orbital quantities (see Gregory 2005). The initial error assumed for the photometric measurements is 1.6 millimagnitudes (mmag), which is approximately the out-of-eclipse scatter, and the initial errors for the velocities are those listed in Table 2. The large scatter in the phase-folded photometry compared to the typical precision of the *K2* instrument (roughly 50 parts per million per half-hour integration for a non-variable star of this brightness) is caused by obvious distortions presumably due to spots, which appear to be changing on very short timescales of days. This is illustrated in Figure 4, and discussed further below.

Initial tests showed that the second-order limb-darkening coefficients q_2 were essentially unconstrained for both stars, likely because of the light curve distortions just mentioned. We therefore held those coefficients fixed at their theoretical values for the *Kepler* band according

to Claret & Bloemen (2011), selecting the ones based on ATLAS model atmospheres and the least-squares fitting procedure favored by those authors. The tabulated u_2 values in the standard quadratic limb-darkening formulation are 0.305 and 0.182 for the primary and secondary. For the linear coefficients q_1 we adopted Gaussian priors from theory with a standard deviation of 0.1 (see Table 4). We also found that while the albedo for the secondary was well constrained, the one for the primary was not. We chose to impose weak Gaussian priors on both, with a mean of 0.5 (appropriate for convective stars) and a standard deviation of 0.3. Finally, all our tests indicated a negligible eccentricity for the inner orbit, consistent with the findings from the spectroscopy. To reduce the already large number of free parameters, we set the eccentricity to zero for the remainder of this work.

The results of our analysis for EPIC 219552514 are reported in Table 4, in which the values given correspond to the mode of the posterior distributions. The distributions of the derived quantities listed in the bottom section of the table were constructed directly from the MCMC chains of the adjustable parameters involved. Included among these is J_{ave} , the surface brightness ratio averaged over the stellar disk, and the flux ratio ℓ_2/ℓ_1 in the *Kepler* band. Both stars in the inner binary are found to be nearly spherical, justifying the use of this binary model. We calculate the oblateness of the primary star as defined by Binnendijk (1960) to be 0.008, which is well below the safe limit for this binary model (0.04; see, e.g., Popper & Etzel 1981). The oblateness of the secondary is an order of magnitude smaller.

The observations and final model are shown in Figure 5. As noted earlier, we attribute the considerable scatter of the residuals (just under 1.6 mmag) to photometric modulation from spots rotating in and out of view. The nature of this scatter is highly correlated (“red”) noise, which raises at least two concerns. On the one hand, it could introduce possibly significant biases in the results. On the other, it will generally cause the formal uncertainties from our MCMC analysis to be underestimated. We now address each of these issues in turn.

To gain an understanding of the extent to which these distortions may affect the fitted parameters, we divided the complete *K2* data set into 29 separate cycles each containing one primary and one secondary eclipse (for an average of 125 data points per cycle), with the last cycle including an extra primary eclipse. We repeated the analysis independently for each cycle in the same way as above, except that we added a 4-term Fourier series to the model (9 extra parameters) in order to at least partially account for the distortions, and we used only the photometry for computational expediency. The fundamental period was kept fixed at the orbital period, which along with the mass ratio was adopted from our model results in Table 4. The median value for each parameter over the 29 data segments, and the corresponding 68.3% confidence intervals, are given in Table 5. Comparison with the values in Table 4 indicates very good agreement for the geometric parameters $r_1 + r_2$, k , and $\cos i$, which are the most relevant here. From this we conclude that any detrimental effect of the lightcurve distortions seems to average out over the 29 cycles, at least in this particular case. The agreement is in fact also good for all

⁹ <http://dan.iel.fm/emcee>

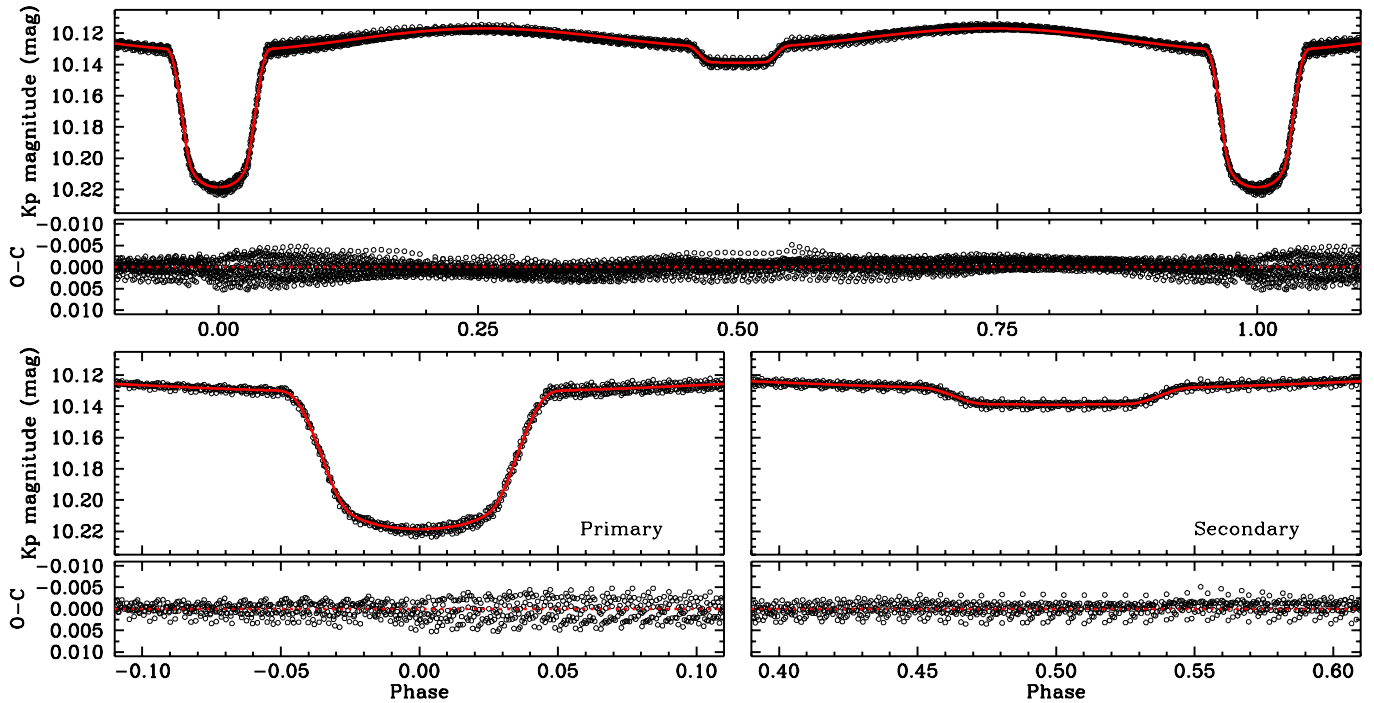


Figure 5. *K2* observations of EPIC 219552514 along with our adopted model. Enlargements of the eclipses are shown at the bottom. Residuals in magnitude units are displayed on an expanded scale below each panel.

other parameters in Table 5 except for the limb darkening coefficient of the secondary, and to a lesser degree its albedo. These may well be biased in Table 4, but have no influence on any other results. The addition of the 4-term Fourier series to the model for each cycle clearly improves the solutions considerably, reducing the typical scatter by a factor of more than 6 compared to our original fit, from about 1.6 mmag to ~ 0.4 mmag. This is still larger than what the instrument is capable of delivering because the lightcurve distortions are far from regular.

To address the possibility of underestimated uncertainties, we carried out a residual permutation exercise in a similar way as done for our previous two studies in Paper I and Paper II. We generated many synthetic data sets by shifting the photometric residuals from our adopted model by an arbitrary number of time indices, and adding them back into the model curve at each time of observation (with wrap-around). We then performed a new MCMC analysis on each set, in each case using slightly perturbed values for quantities that had been held fixed in our original analysis (the second-order limb darkening coefficients, and the gravity darkening coefficients). The perturbed quantities were generated by adding Gaussian noise to the values from theory with standard deviations of 0.10 for u_2 and 0.05 for y_1 and y_2 . We repeated this 100 times, and adopted the scatter (standard deviation) of the resulting distribution for each fitted parameter as a more realistic measure of the uncertainty. These numbers were added quadratically to the internal errors from our original MCMC analysis, resulting in the final uncertainties reported in Table 4. The parameters that had their internal errors inflated the most are J , k , q_1 for the primary, and the albedo A_2 for the secondary, by factors typically ranging from 3 to about 7. In other cases, the extra error is similar to or smaller than the internal errors.

4. ABSOLUTE DIMENSIONS

The physical properties we infer for the components of EPIC 219552514 are presented in Table 6, in which the values listed correspond to the mode of the posterior distributions calculated by directly combining the chains of adjusted parameters in the top section of Table 4. The uncertainties represent the 68.3% confidence intervals. The precision in the absolute masses is 4.2% for the primary and 2.3% for the secondary, while the radii have errors of 1.2% and 2.0%, respectively. Included among the physical parameters are the luminosities, the absolute bolometric and visual magnitudes, and the distance to the system (determined to about 7.7%). For derived quantities involving external information, those external quantities (effective temperatures, bolometric corrections, interstellar reddening, and the apparent visual magnitude of the system; see below) were assumed to be distributed normally and independently for combining them with the chains of adjusted parameters.

In Section 2.2 we derived an estimate of the primary temperature directly from our spectra (6180 ± 100 K), but had to use an adopted value for the much fainter secondary (4000 K) for the radial-velocity determinations. Our analysis of the light curve now provides an accurate way to measure the temperature ratio (or difference, ΔT_{eff}) between the components, through the central surface parameter J (or the disk-integrated value J_{ave} ; Table 4). This, then, allows the secondary temperature to be inferred. Such estimates are often quite accurate because J is closely related to the difference in depth between the eclipses, which can be measured accurately. We obtain $\Delta T_{\text{eff}} = 2170 \pm 140$ K, with which the secondary temperature becomes 4010 ± 170 K. This is essentially the same as the value adopted in Section 2.2 for the radial-velocity determinations, justifying that choice a posteriori. We adopt this as the final temperature of

Table 4
Results from our Combined MCMC Analysis for
EPIC 219552514

Parameter	Value	Prior
P_{in} (days).....	$2.7535724^{+0.000019}_{-0.000024}$	[2, 3]
T_0 (HJD-2,400,000)	$57357.79215^{+0.00019}_{-0.00018}$	[57356, 57358]
J	$0.107^{+0.014}_{-0.014}$	[0.02, 1.0]
$r_1 + r_2$	$0.2949^{+0.0011}_{-0.0010}$	[0.01, 0.50]
k	$0.2603^{+0.0038}_{-0.0035}$	[0.1, 1.0]
$\cos i$	$0.002^{+0.018}_{-0.002}$	[0, 1]
m_0 (mag)	$10.11773^{+0.00030}_{-0.00032}$	[9, 11]
Primary q_1	$0.325^{+0.064}_{-0.064}$	$G(0.198, 0.1)$
Secondary q_1	$0.554^{+0.104}_{-0.090}$	$G(0.344, 0.1)$
A_1	$0.66^{+0.24}_{-0.34}$	$G(0.5, 0.3)$
A_2	$0.35^{+0.12}_{-0.12}$	$G(0.5, 0.3)$
ℓ_3	$0.000^{+0.025}_{-0.000}$	[-10, 0]*
γ (km s ⁻¹)	$+41.338^{+0.057}_{-0.038}$	[30, 50]
K_1 (km s ⁻¹)	$58.964^{+0.058}_{-0.045}$	[1, 180]
K_2 (km s ⁻¹)	$137.2^{+2.5}_{-2.1}$	[1, 180]
ΔRV (km s ⁻¹)	$-0.8^{+1.5}_{-1.5}$	[-10, 10]
P_{out} (days)	$463.5^{+2.4}_{-2.5}$	[200, 800]
T_{peri} (HJD-2,400,000) ...	$58076.9^{+5.4}_{-4.2}$	[57900, 58600]
K_{out} (km s ⁻¹)	$5.436^{+0.073}_{-0.074}$	[1, 180]
$\sqrt{e_{\text{out}}} \cos \omega_{\text{out}}$	$-0.016^{+0.024}_{-0.033}$	[-1, 1]
$\sqrt{e_{\text{out}}} \sin \omega_{\text{out}}$	$+0.437^{+0.019}_{-0.020}$	[-1, 1]
f_{K2}	$0.980^{+0.044}_{-0.044}$	[-5, 1]*
f_1	$1.06^{+0.16}_{-0.11}$	[-5, 5]*
f_2	$0.945^{+0.162}_{-0.092}$	[-5, 5]*
Derived quantities		
r_1	$0.23386^{+0.00099}_{-0.00091}$...
r_2	$0.06087^{+0.00085}_{-0.00075}$...
i (degree)	$89.91^{+0.09}_{-1.02}$...
Eclipse duration (hour) ..	$6.292^{+0.024}_{-0.021}$...
Primary u_1	$0.265^{+0.044}_{-0.044}$...
Secondary u_1	$0.58^{+0.10}_{-0.13}$...
J_{ave}	$0.096^{+0.013}_{-0.013}$...
ℓ_2/ℓ_1	$0.00751^{+0.00066}_{-0.00065}$...
e_{out}	$0.191^{+0.018}_{-0.016}$...
ω_{out} (degree)	$92.2^{+4.3}_{-3.1}$...

Note. — The values listed correspond to the mode of the respective posterior distributions, and the uncertainties represent the 68.3% credible intervals. Priors in square brackets are uniform over the specified ranges, except those for ℓ_3 , f_{K2} , f_1 , and f_2 (marked with asterisks), which are log-uniform. For the first order limb-darkening coefficients and the albedos the priors were Gaussian, indicated above as $G(\text{mean}, \sigma)$.

the secondary, and list it in Table 6.

The component temperatures may be used to derive an estimate of the reddening, as done in our earlier studies of Paper I and Paper II. We refer the reader to those sources for the details. Briefly, we gathered standard photometry for the combined light of EPIC 219552514 in

Table 5
Results from our cycle-by-cycle MCMC
Analysis for EPIC 219552514 with the addition
of a 4-term Fourier series to the model

Parameter	Value
J	$0.0907^{+0.0074}_{-0.0080}$
$r_1 + r_2$	$0.29474^{+0.00063}_{-0.00068}$
k	$0.25962^{+0.00092}_{-0.00067}$
$\cos i$	$0.00197^{+0.00053}_{-0.00093}$
Primary q_1	$0.330^{+0.024}_{-0.015}$
Secondary q_1	$0.3514^{+0.0101}_{-0.0085}$
A_1	$0.508^{+0.031}_{-0.019}$
A_2	$0.533^{+0.058}_{-0.067}$
ℓ_3	$0.00015^{+0.00005}_{-0.00004}$
f_{K2}	$0.151^{+0.020}_{-0.026}$
Derived quantities	
r_1	$0.23400^{+0.00059}_{-0.00053}$
r_2	$0.06066^{+0.00015}_{-0.00019}$
i (degree)	$89.887^{+0.053}_{-0.030}$
Primary u_1	$0.270^{+0.022}_{-0.013}$
Secondary u_1	$0.4204^{+0.0086}_{-0.0118}$
J_{ave}	$0.0917^{+0.0062}_{-0.0077}$
ℓ_2/ℓ_1	$0.00735^{+0.00036}_{-0.00029}$

Note. — The values listed correspond to the median of the results for the 29 independent orbital cycles. The uncertainties represent the 68.3% credible intervals.

the Tycho-2, Johnson, Sloan, 2MASS, and *Gaia* systems (Høg et al. 2000; Henden et al. 2015; Skrutskie et al. 2006; *Gaia* Collaboration et al. 2018) and we constructed 14 non-independent color indices. We then used color/temperature calibrations by Casagrande et al. (2010), Huang et al. (2015), and Stassun et al. (2019) to derive an average photometric temperature for a range of reddening values, adjusting all color indices appropriately at each value of $E(B - V)$. Our adopted reddening estimate is the one that provides a match to the luminosity-weighted average temperature of the binary system. We ignored the presence of the tertiary, as it is faint enough that it will not affect the results. We obtained $E(B - V) = 0.119 \pm 0.025$ mag, corresponding to $A_V = 0.369 \pm 0.078$ mag for a ratio of total to selective extinction of $R_V = 3.1$. Very similar values were found for the other two eclipsing binaries studied previously in the cluster.

A consistency check on our effective temperatures and radii may be obtained by comparing our measured flux ratios with predicted values from synthetic spectra. Figure 6 shows the predictions as a function of wavelength, using spectra by Husser et al. (2013) based on PHOENIX model atmospheres for temperatures of 6200 K and 4000 K, near our best estimates for the binary components. The normalization of the ratio of the spectra was carried out with the radius ratio derived from our light curve analysis, $k = 0.260$. Our measured flux ratios from spectroscopy and from the $K2$ photometry show very good agreement with the expected val-

Table 6
Physical Properties of EPIC 219552514

Parameter	Primary	Secondary
M ($\mathcal{M}_{\odot}^{\text{N}}$)	$1.509^{+0.063}_{-0.056}$	$0.649^{+0.015}_{-0.014}$
R ($\mathcal{R}_{\odot}^{\text{N}}$)	$2.505^{+0.026}_{-0.031}$	$0.652^{+0.013}_{-0.012}$
$\log g$ (dex)	$3.8216^{+0.0093}_{-0.0090}$	$4.624^{+0.011}_{-0.012}$
$q \equiv M_2/M_1$	$0.4296^{+0.0070}_{-0.0077}$	
a ($\mathcal{R}_{\odot}^{\text{N}}$)	$10.69^{+0.13}_{-0.12}$	
T_{eff} (K)	6180 ± 100	4010 ± 170
L (L_{\odot})	$8.19^{+0.61}_{-0.52}$	$0.096^{+0.021}_{-0.013}$
M_{bol} (mag)	$2.442^{+0.077}_{-0.072}$	$7.22^{+0.21}_{-0.17}$
BC_V (mag)	-0.023 ± 0.100	-1.131 ± 0.100
M_V (mag)	$2.47^{+0.12}_{-0.12}$	$8.37^{+0.22}_{-0.21}$
$v_{\text{sync}} \sin i$ (km s^{-1}) ^a	$46.01^{+0.48}_{-0.56}$	$11.98^{+0.23}_{-0.23}$
$v \sin i$ (km s^{-1}) ^b	49 ± 3	12 (adopted)
$E(B - V)$ (mag)	0.119 ± 0.025	
A_V (mag)	0.369 ± 0.078	
Dist. modulus (mag)	$7.33^{+0.15}_{-0.15}$	
Distance (pc)	291^{+22}_{-18}	
π (mas)	$3.39^{+0.26}_{-0.21}$	
$\pi_{\text{Gaia}/\text{DR2}}$ (mas) ^c	3.671 ± 0.052	

Note. — The masses, radii, and semimajor axis a are expressed in units of the nominal solar mass and radius ($\mathcal{M}_{\odot}^{\text{N}}$, $\mathcal{R}_{\odot}^{\text{N}}$) as recommended by 2015 IAU Resolution B3 (see Prša et al. 2016), and the adopted solar temperature is 5772 K (2015 IAU Resolution B2). Bolometric corrections are from the work of Flower (1996), with conservative uncertainties of 0.1 mag, and the bolometric magnitude adopted for the Sun appropriate for this BC_V scale is $M_{\text{bol}}^{\odot} = 4.732$ (see Torres 2010). See text for the source of the reddening. For the apparent visual magnitude of EPIC 219552514 out of eclipse we used $V = 10.164 \pm 0.026$ (Henden et al. 2015). The flux of the tertiary component is ignored here.

^a Synchronous projected rotational velocity assuming spin-orbit alignment.

^b Measured projected rotational velocity for the primary.

^c A global parallax zero-point correction of +0.029 mas has been added to the parallax (Lindgren et al. 2018a), and 0.021 mas added in quadrature to the internal error (see Lindgren et al. 2018b).

ues, supporting the accuracy of our determinations for EPIC 219552514.

The measured projected rotational velocity for the primary star, $v \sin i = 49 \pm 3 \text{ km s}^{-1}$, agrees with the predicted value $v_{\text{sync}} \sin i$ listed in Table 6, which assumes synchronous rotation and spin-orbit alignment. Given the ~ 2.7 Gyr age of the parent cluster, this is as expected from tidal theory (see, e.g. Hilditch 2001), which indicates synchronization should occur on a timescale of less than 2 Myr. The negligible eccentricity we find for the inner orbit is also consistent with the expectation that tidal forces should circularize it on a timescale of about 300 Myr, much shorter than the cluster age.

The elements we derive for the outer orbit, along with the absolute masses for the binary components, imply a minimum mass for the tertiary star of about $0.36 M_{\odot}$. If it is a main sequence star, the lack of detection in our spectra implies a mass that can be no larger than that of the secondary, or $\sim 0.65 M_{\odot}$. This, in turn, gives a lower limit for the inclination angle of the outer orbit of about

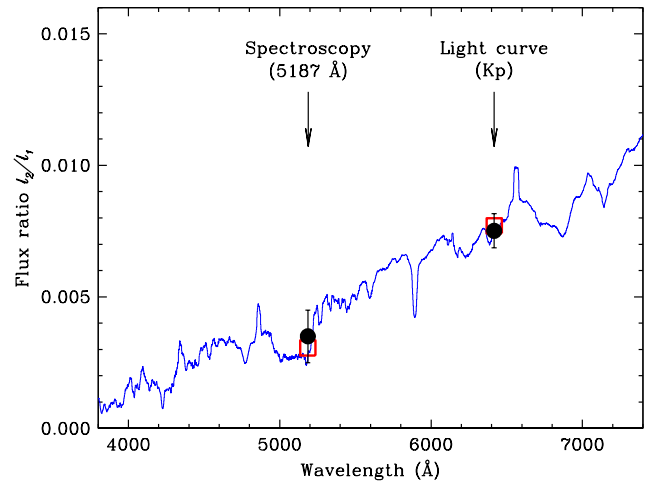


Figure 6. Comparison of the predicted flux ratio between the components of EPIC 219552514 and our ℓ_2/ℓ_1 values measured spectroscopically and from the light curve analysis. Squares represent the calculated flux ratio integrated over the corresponding spectroscopic and $K2$ bandpasses, and the measurements are shown as circles with error bars. The calculated curve is based on model spectra by Husser et al. (2013) for solar metallicity, normalized using our measured radius ratio $k = 0.260$. For the primary we used $T_{\text{eff}} = 6200$ K and $\log g = 4.0$, and for the secondary $T_{\text{eff}} = 4000$ K and $\log g = 4.5$.

34° . Alternatively, the tertiary may be a white dwarf.

4.1. Rotation and activity

Oscillations in the $K2$ photometry of EPIC 219552514 are obvious in the residuals from our light curve analysis, and are seen as a function of time in the top panel of Figure 7. The oscillations are rather irregular (see also Figure 4), and display a peak-to-peak amplitude close to 10 mmag. This amplitude is in line with those seen in other late F dwarfs, as reported by Giles et al. (2017). A Lomb-Scargle periodogram of the residuals shows a main peak at a period of 2.81 ± 0.04 days (bottom panel of Figure 7), which we interpret as a rotational signature caused by one or more spots or spot regions. The uncertainty was estimated from the half width of the peak at half maximum. This period is marginally longer than the 2.75-day orbital period of the binary, which could imply subsynchronous rotation, or may also be a consequence of solar-like differential rotation, with spots located at intermediate or high latitudes rotating more slowly than the equator. In view of the spectroscopic evidence ($v \sin i$ of the primary) presented earlier for spin-orbit synchronization, we are inclined to favor the latter interpretation. The spots are most likely located on the primary star, as assuming that they are on the secondary would imply a rather unusual intrinsic amplitude exceeding one magnitude, because of the large brightness dilution factor ($\ell_2/\ell_1 \approx 0.0075$).

While spot modulation is often associated with other indicators of stellar activity, examination of the spectra for EPIC 219552514 has revealed no evidence of Ca II H and K emission, or variable $H\alpha$ equivalent widths. This is perhaps consistent with the relatively small amplitude of the photometric variations. We note also that, as far as we can tell, the object does not appear to have been detected as an X-ray source (e.g., by *ROSAT*; Voges et al. 1999) or as a source of ultraviolet radiation (*GALEX*; Bianchi et al. 2011). It would not be surprising if the

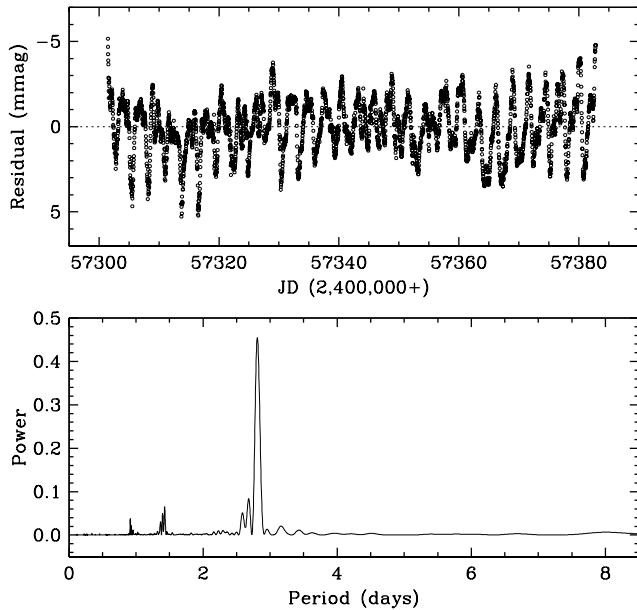


Figure 7. Residuals from our best fit to the *K2* photometry of EPIC 219552514 showing modulations presumably due to spots. The corresponding periodogram shown at the bottom features a dominant peak at a period of $P_{\text{rot}} = 2.81 \pm 0.04$ days.

faint secondary star were somewhat active as well, despite the old age of the system, given its moderately large expected rotational velocity of about 12 km s^{-1} (Table 4).

5. COMPARISON WITH THEORY

The masses, radii, and temperatures of the binary components of EPIC 219552514 are compared in Figure 8 against models of stellar evolution from the PARSEC v1.2S series by Chen et al. (2014). Isochrones in both the mass-radius and mass-temperature diagrams are shown for the age range 2.0–3.2 Gyr in steps of 0.2 Gyr, with the heavy dashed line representing the best fit. The corresponding age is $2.67^{+0.39}_{-0.55}$ Gyr, in which the uncertainty is dominated by the error in the primary mass. Uncertainties in the adopted chemical composition of Ruprecht 147 ($[\text{Fe}/\text{H}] = +0.10 \pm 0.04$; see Curtis et al. 2018) contribute an additional 0.13 Gyr to the error budget for the age.

Because the age determination for EPIC 219552514 is only sensitive to the radius of the primary star (the secondary evolves too slowly), the best-fit isochrone matches R_1 precisely. The secondary radius appears slightly larger than predicted (by 3.7%), although the deviation is less than twice its uncertainty and may not be significant. On the other hand, the effective temperatures of both components are consistent with predictions from theory. Many cool main sequence stars such as the secondary have shown discrepancies with standard stellar evolution models that are believed to be caused by stellar activity (see, e.g., Torres 2013). They tend to be larger and cooler than predicted. However, in this case a reasonably good agreement between the $[R, T_{\text{eff}}]$ measurements for the secondary and these particular models is expected a priori because the PARSEC v1.2S models have been adjusted by changing the temperature-opacity relation in such a way as to match the average measured properties of low-mass stars (see Chen et al. 2014).

The above age determination for EPIC 219552514

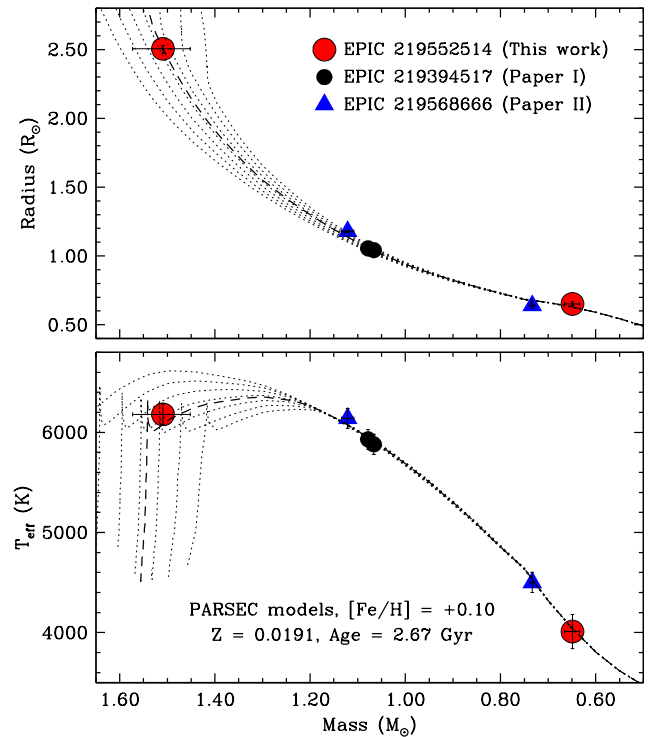


Figure 8. Physical properties of EPIC 219552514 compared against model isochrones from the PARSEC v1.2S series (Chen et al. 2014) for the metallicity of the cluster, $[\text{Fe}/\text{H}] = +0.10$. The dotted lines in both panels represent isochrones for ages between 2.0 and 3.2 Gyr in steps of 0.2 Gyr, and the heavy dashed line corresponds to an age of 2.67 Gyr that fits the measured masses and radii best. Results for the two eclipsing binaries studied previously in Paper I and Paper II are shown as well.

agrees well with our estimates for the eclipsing binaries EPIC 219394517 and EPIC 219568666 from our earlier studies (Paper I and Paper II), whose physical properties are also shown in the figure.¹⁰ The ages we reported for those two objects using the same PARSEC models as above are 2.65 ± 0.25 and 2.76 ± 0.61 Gyr. Other models with different physical ingredients lead to slightly different ages. For example, using the MIST models of Choi et al. (2016), we obtain a marginally younger age for EPIC 219552514 of 2.51 Gyr.

The evolved status of the primary star places it at the very end of the main sequence for the cluster. This may be seen in the color-magnitude diagram of Figure 9, which shows other member stars from the *Gaia*/DR2 catalog along with the 2.67 Gyr PARSEC isochrone corrected for reddening and extinction. The absolute magnitudes for the other members were calculated using their individual parallaxes. The two previously studied binaries in Ruprecht 147 are marked on the isochrone as well, at the locations expected from their measured masses.

6. FINAL REMARKS

EPIC 219552514 is special for being located near the turnoff of Ruprecht 147, making it the system most sensitive to age among the known eclipsing binaries in the

¹⁰ As discussed in Paper II, the individual component radii for EPIC 219568666 were reported to be slightly affected by systematic errors in the radius ratio k , although the age could still be determined accurately using instead the sum of the radii, which is unaffected.

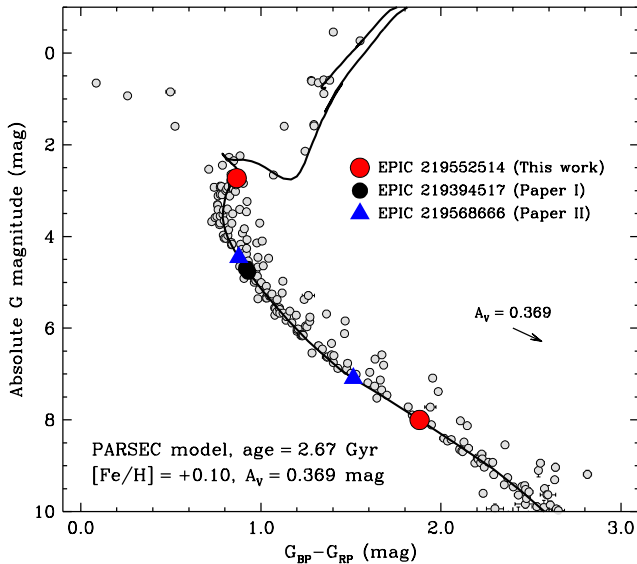


Figure 9. Color-magnitude diagram for Ruprecht 147 based on the measured G magnitudes, $G_{BP} - G_{RP}$ colors, and parallaxes from the *Gaia*/DR2 catalog. Also shown is a model isochrone from the PARSEC series (Chen et al. 2014) for the metallicity of the cluster and the age that best fits the properties of EPIC 219552514 (Figure 8). Reddening and extinction corrections have been applied to the model (reddening vector indicated with an arrow). The same symbols as in Figure 8 are used to mark the locations on the main sequence of the stars in EPIC 219552514 and the other two eclipsing binaries in the cluster studied previously.

cluster. Our accurate mass and radius determinations have allowed an accurate age to be inferred for the binary ($2.67^{+0.39}_{-0.55}$ Gyr) based on the PARSEC models. This is in excellent agreement with estimates for the two previously studied eclipsing systems in the cluster that used the same models. The weighted average of the three determinations is 2.67 ± 0.21 Gyr. The precision of our current age for EPIC 219552514 is limited by the uncertainty in the mass of the primary star (4.2%), which in turn is caused mostly by the reduced precision of the radial velocities of the secondary star on account of its faintness ($\sigma_{RV} \sim 8.5$ km s $^{-1}$, on average). Additional spectra with higher signal-to-noise ratios would help to reduce these statistical errors.

Our distance estimate for EPIC 219552514 is similar to those inferred in Paper I and Paper II, and implies a parallax ($3.39^{+0.26}_{-0.21}$ mas) that is marginally lower than the one reported in the *Gaia*/DR2 catalog (3.671 ± 0.051 mas), although still consistent within the errors. It is possible that part of the difference is due to the fact that the system is found here to be triple, whereas *Gaia* has so far been treating the object as a single star. The discovery that EPIC 219552514 is a triple system is in fact not surprising, as it has been found that the vast majority of spectroscopic binaries with periods under 3 days have additional companions (96%, according to Tokovinin et al. 2006).

The nature of the third component, i.e., whether it is a main-sequence star or a white dwarf, is undetermined from the present data. In either case, this distant companion may play a role in the dynamical evolution of the system, modulating the eccentricity of the inner eclipsing binary (which we currently find to be consistent with having a circular orbit) as well as modulat-

ing the relative inclination angle between the inner and outer orbital planes (Kozai-Lidov oscillations; see, e.g., Naoz 2016). The latter can potentially change the eclipse depths, or temporarily cause them to cease altogether. This would be expected to occur on timescales that are much longer than the orbital periods. We find the system to be dynamically stable according to the criteria of Eggleton & Kiseleva (1995) and Mardling & Aarseth (2001), for any reasonable mass of the third star and any relative inclination of the orbital planes.

If the tertiary is a white dwarf, constraints on its mass and that of its progenitor may be obtained from the same PARSEC isochrone used earlier for the age and metallicity of Ruprecht 147. We find a lower limit for the progenitor mass of $1.59 M_{\odot}$, and a corresponding lower limit for the present-day white dwarf mass of $0.60 M_{\odot}$. This would imply significant mass loss from the third component, which may have left some observable trace on the system. One possibility would be chemical pollution of the eclipsing binary components. This could be pursued through a detailed spectroscopic analysis of the primary star.

We estimate the angular size of the outer orbit to be about 5.7 mas at the distance of Ruprecht 147, which is inside the reach of our NRM observations described in Section 2.3. While *Gaia* cannot spatially resolve the tertiary, in principle it should be capable of detecting the motion of the eclipsing binary in the outer orbit with a period of 463 days. We estimate this motion should have a semimajor axis between 0.8 and 1.3 mas, depending on the outer inclination angle, assuming the tertiary contributes negligibly to the total light. Disappointingly, the *Gaia*/DR2 data for this system show no sign of excess astrometric noise (which could otherwise be an indication of unmodeled motion), although it is still possible that the 463 day signal may emerge or be recoverable by the end of the mission, particularly with the knowledge we now have. In that case, *Gaia* should be able to measure the inclination angle of the outer orbit. When combined with the elements of our spectroscopic orbit, this angle would then immediately allow a determination of the dynamical mass of the tertiary component.

The spectroscopic observations of EPIC 219552514 were gathered with the help of P. Berlind, M. Calkins, and G. Esquerdo. J. Mink is thanked for maintaining the CfA echelle database. The anonymous referee provided helpful comments on the original manuscript. G.T. acknowledges partial support from NASA’s Astrophysics Data Analysis Program through grant 80NSSC18K0413, and to the National Science Foundation (NSF) through grant AST-1509375. J.L.C. is supported by the NSF Astronomy and Astrophysics Postdoctoral Fellowship under award AST-1602662, and by NASA under grant NNX16AE64G issued through the *K2* Guest Observer Program (GO 7035). The research has made use of the SIMBAD and VizieR databases, operated at the CDS, Strasbourg, France, and of NASA’s Astrophysics Data System Abstract Service. The work has also made use of data from the European Space Agency (ESA) mission *Gaia* (<https://www.cosmos.esa.int/gaia>), processed by the *Gaia* Data Processing and Analysis Consortium (DPAC, <https://www.cosmos.esa.int/web/>

gaia/dpac/consortium). Funding for the DPAC has been provided by national institutions, in particular the institutions participating in the *Gaia* Multilateral Agreement. The computational resources used for this research include the Smithsonian Institution’s “Hydra” High Performance Cluster.

REFERENCES

- Andersen, J. 1991, *A&A Rev.*, 3, 91
- Bianchi, L., Herald, J., Efremova, B., et al. 2011, *Ap&SS*, 335, 161
- Binnendijk, L. 1960, *Properties of Double Stars*, (Univ. of Pennsylvania Press: Philadelphia), p. 290
- Casagrande, L., Ramírez, I., Meléndez, J., Bessell, M., & Asplund, M. 2010, *A&A*, 512, A54
- Chen, Y., Girardi, L., Bressan, A., et al. 2014, *MNRAS*, 444, 2525
- Choi, J., Dotter, A., Conroy, C., et al. 2016, *ApJ*, 823, 102
- Claret, A., & Bloemen, S. 2011, *A&A*, 529, A75
- Curtis, J. L., Vanderburg, A., Torres, G., et al. 2018, *AJ*, 155, 173
- Curtis, J. L. 2016, PhD Thesis, Penn State University
- Curtis, J. L., Wolfgang, A., Wright, J. T., Brewer, J. M., & Johnson, J. A. 2013, *AJ*, 145, 134
- Eggleton, P., & Kiseleva, L. 1995, *ApJ*, 455, 640
- Etzel, P. B. 1981, *Photometric and Spectroscopic Binary Systems*, Proc. NATO Adv. Study Inst., ed. E. B. Carling & Z. Kopal (Dordrecht: Reidel), p. 111
- Flower, P. J. 1996, *ApJ*, 469, 355
- Foreman-Mackey, D., Hogg, D. W., Lang, D., & Goodman, J. 2013, *PASP*, 125, 306
- Fűrész, G. 2008, PhD thesis, Univ. Szeged, Hungary
- Gaia Collaboration, Brown, A. G. A., Vallenari, A. et al. 2018, *A&A*, 616, 1
- Gelman, A., & Rubin, D. B. 1992, *Statistical Science*, 7, 457
- Giles, H. A. C., Collier Cameron, A., & Haywood, R. D. 2017, *MNRAS*, 472, 1618
- Gilliland, R. L., Jenkins, J. M., Borucki, W. J., et al. 2010, *ApJ*, 713, L160
- Goodman, J., & Weare, J. 2010, *Commun. Appl. Math. Comput. Sci.*, 5, 65
- Gregory, P. C. 2005, *ApJ*, 631, 1198
- Henden, A. A., Levine, S., Terrell, D., & Welch, D. L. 2015, *American Astronomical Society Meeting Abstracts #225*, 225, 336.16
- Hilditch, R. W. 2001, *An Introduction to Close Binary Stars* (Cambridge, UK: Cambridge University Press) p. 152
- Høg, E., Fabricius, C., Makarov, V. V., et al. 2000, *A&A*, 355, L27
- Hora, J. L., Luppini, G. A., & Hodapp, K.-W. 1994, *Proc. SPIE*, 2198, 498
- Huang, Y., Liu, X.-W., Yuan, H.-B., et al. 2015, *MNRAS*, 454, 2863
- Husser, T.-O., Wende-von Berg, S., Dreizler, S., et al. 2013, *A&A*, 553, A6
- Ireland, M. J. 2013, *MNRAS*, 433, 1718
- Irwin, J. M., Quinn, S. N., Berta, Z. K., et al. 2011, *ApJ*, 742, 123
- Kipping, D. M. 2010, *MNRAS*, 408, 1758
- Kipping, D. M. 2013, *MNRAS*, 435, 2152
- Kraus, A. L., Ireland, M. J., Huber, D., Mann, A. W., & Dupuy, T. J. 2016, *AJ*, 152, 8
- Kraus, A. L., Ireland, M. J., Martinache, F., & Lloyd, J. P., *ApJ*, 679, 762
- Latham, D. W., Stefanik, R. P., Torres, G., et al. 2002, *AJ*, 124, 1144
- Lindgren, L., Hernández, J., Bombrun, A., et al. 2018a, *A&A*, 616, A2
- Lindgren, L., Hernández, J., Bombrun, A., et al. 2018b, *Gaia DR2 astrometry presentation*, https://www.cosmos.esa.int/documents/29201/1770596/Lindgren_GaiaDR2_Astrometry_extended.pdf/1ebddb25-f010-6437-cb14-0e360e2d9f09, p. 35
- Mardling, R. A., & Aarseth, S. J. 2001, *MNRAS*, 321, 398
- Naoz, S. 2016, *ARA&A*, 54, 441
- Nordström, B., Latham, D. W., Morse, J. A., et al. 1994, *A&A*, 287, 338
- Olivares, J., Bouy, H., Sarro, L. M., et al. 2019, *A&A*, 625, A115
- Popper, D. M., & Etzel, P. B. 1981, *AJ*, 86, 102
- Prša, A., Harmanec, P., Torres, G., et al. 2016, *AJ*, 152, 41
- Skrutskie, M. F., Cutri, R. M., Stiening, R., et al. 2006, *AJ*, 131, 1163
- Stassun, K. G., Oelkers, R. J., Paegert, M., et al. 2019, *AJ*, 158, 138
- Szentgyorgyi, A. H., & Fűrész, G. 2007, *Precision Radial Velocities for the Kepler Era*, in *The 3rd Mexico-Korea Conference on Astrophysics: Telescopes of the Future and San Pedro Mártir*, ed. S. Kurtz, RMxAC, 28, 129
- Tokovinin, A., Thomas, S., Sterzik, M., et al. 2006, *A&A*, 450, 681
- Torres, G. 2010, *AJ*, 140, 1158
- Torres, G. 2013, *Astronomische Nachrichten*, 334, 4
- Torres, G., Andersen, J., & Giménez, A. 2010, *A&A Rev.*, 18, 67
- Torres, G., Curtis, J. L., Vanderburg, A., Kraus, A. L., & Rizzuto, A. 2018, *ApJ*, 866, 67 (Paper I)
- Torres, G., McGruder, C. D., Siverd, R. J., et al. 2017, *ApJ*, 836, 177
- Torres, G., Neuhäuser, R., & Guenther, E. W. 2002, *AJ*, 123, 1701
- Torres, G., Vanderburg, A., Curtis, J. L., et al. 2019, *ApJ*, 887, 109 (Paper II)
- Vanderburg, A., & Johnson, J. A. 2014, *PASP*, 126, 948
- Vanderburg, A., Latham, D. W., Buchhave, L. A., et al. 2016, *ApJS*, 222, 14
- Voges, W., Aschenbach, B., Boller, T., et al. 1999, *A&A*, 349, 389
- Yeh, F. C., Carraro, G., Montalto, M., et al. 2019, *AJ*, 157, 115
- Zucker, S., & Mazeh, T. 1994, *ApJ*, 420, 806
- Zucker, S., Torres, G., & Mazeh, T. 1995, *ApJ*, 452, 863